Nonlinear unmixing of hyperspectral images using multiple kernel self-organizing maps

Shaheera Rashwan[1], *Nicolas Dobigeon*[2], *Walaa Sheta*[1] *and Hanan Hassan*[1]

[1] *Informatics Research Institute, SRTA City, Alexandria, Egypt*
[2] *University of Toulouse, IRIT/INP-ENSEEIHT, 31071 Toulouse Cedex 7, France*
* *E-mail: srashwan@enseeiht.fr*

Abstract: Spatial pixel resolution of common multispectral and hyperspectral sensors is generally not sufficient to avoid that multiple elementary materials contribute to the observed spectrum of a single pixel. To alleviate this limitation, spectral unmixing is a by-pass procedure which consists in decomposing the observed spectra associated with these mixed pixels into a set of component spectra, or endmembers, and a set of corresponding proportions, or abundances, that represent the proportion of each endmember in these pixels. In this paper, a spectral unmixing technique is proposed to handle the challenging scenario of nonlinear mixtures. This algorithm relies on a dedicated implementation of multiple kernel learning using self-organizing map proposed as a solver for the nonlinear unmixing problem. Based on a priori knowledge of the endmember spectra, it aims at estimating their relative abundances without specifying the nonlinear model under consideration. It is compared to state-of the art algorithms using synthetic yet realistic and real hyperspectral images. Results obtained from experiments conducted on synthetic and real hyperspectral images assess the potential and the effectiveness of this unmixing strategy. Finally, the relevance and potential parallel implementation of the proposed method is demonstrated.

1 Introduction

With the recent and rapid development of hyperspectral imaging technology, hyperspectral images have been widely used in various scientific fields, such as environmental mapping, risk prevention, urban planning, pollution monitoring and mining exploration [1]. Even if classical processing tasks of hyperspectral image analysis include dimensionality reduction, object detection and image segmentation/classification, spectral unmixing certainly remains the most investigated technique to extract relevant information from the observed scene while facing with the generally limited spatial resolution of the sensors. Indeed, the raw spatial resolution of standard hyperspectral sensors usually leads to observing mixed pixels, i.e., which are composed of more than one elementary material. Separating these mixed pixels into a set of elementary material spectral signatures (or *endmembers*) and estimating their corresponding fractions (or *abundances*) in each pixel is an automated procedure known as *spectral unmixing* or *spectral mixture analysis* [2].

There are two main classes of mixing models commonly advocated to relate the observed pixel spectrum to the endmember spectra and abundances. The first one, referred to as linear mixing model (LMM), assumes that the observed spectra result from linear combinations of the endmember signatures. Conversely, a wide class of nonlinear mixing models (NLMMs) covers a large variety of applicative contexts where LMM fails to accurately describe the mixing process underlying the observations. Although LMM is easy to implement and to handle in common scenarios, considering NLMM may be inevitable when analyzing more complex scenes, e.g., characterized by multi-layer structures, such as vegetated areas [3] or urban canyons [4], or by intimate sand-like mixtures [5]. The interested reader is invited to consult [6–8] for comprehensive discussions on both classes of models.

Most of the unmixing strategies are based on two-step procedures. Firstly, the spectral signatures associated with the endmembers are extracted from the whole set of image pixels. Secondly, in an inversion step, the abundances are estimated in each pixel based on the estimated endmembers and the adopted linear or nonlinear mixing model. Popular endmember extraction algorithm include N-FINDR [9] and simplex growing algorithm (SGA) [10] which search for a

simplex with the maximum volume inscribed in the dataset. Similarly, pixel purity index (PPI) [11] and vertex component analysis (VCA) [12] recovers this simplex through geometrical projections. Regarding the inversion step, in the past decades, many algorithms based on linear mixed model (LMM) have been developed to recover the abundances associated with each pixel measurement. Heinz and Chang introduced the popular fully constrained least squares (FCLS) unmixing method based on LMM [13]. It is based on a least squares approach that simultaneously exploits the so-called abundance sum-to-one and nonnegativity constraints. More recently, Bioucas-Dias and Figueiredo introduced two algorithms, referred to as Sunsal and C-Sunsal, to solve a class of optimization problems derived from the LMM-based spectral unmixing formulation [14]. The proposed algorithms are based on the alternating direction method of multipliers, which decomposes the initial problem into a sequence of easier ones, with the great advantage of being much more computationally efficient than FCLS.

When dealing with nonlinear mixtures, dedicated unmixing techniques should be considered. Some of them proposed in the literature rely on parametric formulations of the nonlinearities that may occur during the mixing process. When these nonlinearities result from multiple scattering effects, various bilinear mixing models have been designed [15] for which specific unmixing techniques have been developed [4, 16, 17]. Conversely, nonparametric model-based unmixing strategies have been derived to address a larger variety of nonlinear mixtures. When the nonlinearities are considered as additional contributions of the LMM, robust models allows these nonlinear terms to remain unspecified [18, 19]. Additionally, some significant contributions exploit the versatility of the machine learning framework to handle the variety of nonlinear effects, in particular when training dataset are available to learn the nonlinear mapping from the abundances to the measured pixel spectra. For instance, a neural network approach has been proposed in [20] to tackle the unmixing problem by two successive stages: the first one reduces the dimension of the input data, and the second stage performs the mapping from the reduced input data to the abundance coefficients. In [21], extreme learning machines are implemented to train a regression model subsequently resorted to recover the abundances of target

classes.

Besides, multiple-kernel learning (MKL), which is known as learning a kernel machine with a set of basis kernels, has been developed in machine learning area [22] to solve optimization problems arising when conducting a SVM-classification task. MKL can also be envisaged to address unmixing problems. Such a framework has several advantages: i) it can simultaneously use numerous features (computed from the different bands of the hyperspectral images) to enrich the data similarity representations, ii) it is an intermediate combination of data which means that the mixed pixel is preserved during the process without lost of information in its early combinations [22] and iii) it can be easily parallelized to speed up the computation [23]. To this end, Liu *et al.* have proposed a framework called multiple kernel learning-based spectral mixture analysis (MKL-SMA) that integrates a MKL method into the training process of linear spectral mixture analysis [24]. They derived a closed-form solution of the kernel combination parameters unlike most MKL approaches. Similarly, Chen *et al.* have formulated the problem of abundance estimation resulting from nonlinear mixtures based on a multi-kernel learning paradigm [25]. Also, *Gu et al.* [26] have showed that integrating reproducing kernel Hilbert spaces (RKHSs) spanned by a series of different basis kernels in multiple-kernel Hilbert space (MKHS) can empower handling general nonlinear problems more easily than traditional single kernel learning. All these methods are based on MKL with a SVM-based solver. Thus, *per se*, they are supervised learning since they need a priori knowledge on the estimated endmembers and abundances. Unfortunately, in most applicative context, this prior knowledge is not available. To overcome this limitation, this paper suggests to replace the usual solver by neural network, the Kohonen's self-organizing maps (SOMs) [27]. The nonlinear unmixing model proposed in this paper boils down to an appropriate implementation of MK-SOM specifically designed to solve the unmixing problem. This simple and intuitive strategy opens promising routes since, in particular, it is highly parallelizable, which can lead to an easy VLSI implementation based on systolic arrays or FPGAs, and it is easily expendable to a high number of dimensions [28].

The paper is organized as follows. Section 2 presented the proposed multiple kernel SOM (MK-SOM) unmixing strategy, focusing on the training and testing algorithms. Section 3 provides the experimental results we have obtained after applying the proposed methodology to real and synthetic hyperspectral data. Different parameters in the training stage have been considered in order to obtain a detailed description of their influence on the final results. Section 4 describes and illustrates the potential computational gain which can be expected by a parallel implementation of the proposed algorithm on a graphics processing unit (GPU). Finally, section 5 concludes this work.

2 MK-SOM Unmixing

This section details the dedicated implementation of MK-SOM to perform hyperspectral unmixing of possibly nonlinearly mixed pixels. The proposed strategy assumes the endmember spectra have been identified beforehand, based on a priori knowledge regarding the imaged scene of interest, or extracted by a dedicated algorithm (such as VCA).

2.1 General Framework: from SOM to MK-SOM

Let $\mathbf{X} = [\mathbf{x}_1, \ldots, \mathbf{x}_P]$ denote a set of P training pixels $\mathbf{x}_p = [x_{1,p}, \ldots, x_{L,p}]^T$ observed in L spectral bands. The measurements $\{x_{\ell,p}\}_{p \in \mathcal{P}}$ with $\mathcal{P} \triangleq \{1, \ldots, P\}$, i.e., the reflectance of all the pixels observed in the band $\sharp\ell$ with $\ell \in \mathcal{L} \triangleq \{1, \ldots, L\}$, are assumed to live in a given set $\mathbb{X}_\ell$:

$$\forall \ell \in \mathcal{L}, \forall p \in \mathcal{P}, \ x_{\ell,p} \in \mathbb{X}_\ell.$$

Each band $\ell \in \mathcal{L}$ is associated with a known kernel, i.e, a function

$$\mathcal{K}_\ell : \ \mathbb{X}_\ell \times \mathbb{X}_\ell \to \mathbb{R}$$

such that $\mathcal{K}_\ell(\cdot, \cdot)$ is symmetric and positive, i.e.,

$$\forall (x, x') \in \mathbb{X}_\ell \times \mathbb{X}_\ell, \mathcal{K}_\ell(x, x') = \mathcal{K}_\ell(x', x) \quad (1)$$

and

$$\forall \rho \in \mathbb{N}, \ \forall p \leq \rho, \ \forall x_p \in \mathbb{X}_\ell, \ \forall \alpha_p \in \mathbb{R},$$
$$\sum_{i,j} \alpha_i \alpha_j \mathcal{K}_\ell(x_i, x_j) \geq 0. \quad (2)$$

$$\forall (x, x') \in \mathbb{X}_\ell \times \mathbb{X}_\ell, \mathcal{K}_\ell(x, x') = \mathcal{K}_\ell(x', x), \quad (3)$$

$$\forall \rho \in \mathbb{N}, \ \forall p \leq \rho, \ \forall x_p \in \mathbb{X}_\ell, \ \forall \alpha_p \in \mathbb{R}, \sum_{i,j} \alpha_i \alpha_j \mathcal{K}_\ell(x_i, x_j) \geq 0. \quad (4)$$

Popular kernel functions include the linear, Gaussian and polynomial kernels. Then, a new kernel

$$\mathcal{K} : \ \mathbb{X} \times \mathbb{X} \to \mathbb{R} \quad \text{with} \quad \mathbb{X} \triangleq \prod_{\ell=1}^{L} \mathbb{X}_\ell$$

can be introduced as

$$\forall (\mathbf{x}_p, \mathbf{x}_{p'}) \in \mathbb{X} \times \mathbb{X}, \ \mathcal{K}(\mathbf{x}_p, \mathbf{x}_{p'}) = \sum_{\ell=1}^{L} \alpha_\ell \mathcal{K}_\ell(x_{\ell,p}, x_{\ell,p'}) \quad (5)$$

where the set of coefficients $\{\alpha_\ell\}_{\ell \in \mathcal{L}}$ ensures a convex combination

$$\forall \ell \in \mathcal{L} \qquad \alpha_\ell \geq 0, \quad (6)$$
$$\sum_{\ell=1}^{L} \alpha_\ell = 1. \quad (7)$$

As noticed in [29], $\mathcal{K}(\cdot, \cdot)$ is also symmetric and positive. As a consequence, according to the RKHS framework, a function $\phi : \mathbb{X} \to \mathbb{H}$, referred to as the feature map, can be introduced such that

$$\mathcal{K}(\mathbf{x}_p, \mathbf{x}_{p'}) = \langle \phi(\mathbf{x}_p), \phi(\mathbf{x}_{p'}) \rangle \quad (8)$$

and $\mathbb{H}$ is an Hilbert space referred to as the feature space. Traditionally, SOM consists in searching for M so-called neurons or, equivalently, prototypes $\mathbf{p}_m \in \mathbb{H}$ ($m \in \mathcal{M} \triangleq \{1, \ldots, M\}$), to represent the input data $\mathbf{X}$. In other words, a SOM represents the data by a set of prototypes (such as the centroids identified by an unsupervised clustering technique, e.g., K-means), which are topologically organized on a lattice structure. According to the general framework of kernel SOM described in [30], all prototypes are written as convex combinations of the input data in the feature space

$$\forall m \in \mathcal{M}, \ \mathbf{p}_m = \sum_{p=1}^{P} \gamma_{mp} \phi(\mathbf{x}_p) \quad (9)$$

The proposed MK-SOM unmixing algorithm consists of two main steps. First, the training step recovers the pure pixels to obtain the weight map. Then, the testing step computes the abundance vector for each pixel in the image. These two steps are briefly recalled in what follows.

2.2 MK-SOM Training

Following the ideas of [29, 31], we adopt an online implementation of MK-SOM algorithm detailed in Algo 1. The standard (i.e., affectation and representation) steps of the conventional SOM are iteratively applied here for a given total number T of epochs. In particular, the affectation step consists in finding the index k_p of the so-called best-matching unit, i.e., of the closest prototype $\mathbf{p}_m$ of the considered input data $\mathbf{x}_p$. Note that the MK-counterpart of SOM relies on a distance computed in the feature space $\mathbb{H}$ thanks to the associated Gram matrix. Line 8 of Algo. 1, the updating rule involves a neighborhood function $h(\cdot, \cdot)$ chosen as

$$h^{(t)}(m, m') = \exp\left(-\frac{\|\mathbf{p}_m - \mathbf{p}_{m'}\|^2}{2\sigma^{2(t)}}\right) \tag{10}$$

where $\sigma^{2(t)}$ is an algorithmic parameter decreasing along the iterations according to

$$\sigma^{2(t)} = \sigma^{2(t-1)} \exp(-\lambda_{\sigma^2} t) \tag{11}$$

with $\sigma^{2(0)} = 20$ and $\lambda_{\sigma^2} = 0.05$. Moreover, $\mu^{(t)}$ is a learning rate defined as a decreasing function

$$\mu^{(t)} = \mu^{(t-1)} \exp(-\lambda_\mu t) \tag{12}$$

with $\mu^{(0)} = 0.1$ and $\lambda_\mu = 0.05$. Finally, the $\delta(\cdot)$ function stands for the Kronecker operator, i.e., $\delta(j) = 1$ if $j = 0$ and $\delta(j) = 0$ otherwise. In the proposed implementation, the output weight vectors are normalized between the range $(0, 255)$ as the input training and testing vectors have been also normalized [32].

Algorithm 1: MK-SOM unmixing: training step

Input: Training vectors $\mathbf{x}_1, \ldots, \mathbf{x}_P$
Initialization:
Set $\left\{\gamma_{mp}^{(0)}\right\}_{m,p}$ such that $\forall m \in \mathcal{M}, \gamma_{mp}^{(0)} > 0$ and
$\sum_{p=1}^P \gamma_{mp}^{(0)} = 1$
% Initialize all prototypes
for $m = 1, \ldots, M$ **do**
    $\mathbf{p}_m^{(0)} = \sum_{p=1}^P \gamma_{mp}^{(0)} \phi(\mathbf{x}_p)$

1 *% Training* **for** $t = 1, \ldots, T$ **do**
2   **for** $p = 1, \ldots, P$ **do**
3   *% Assignment step*
4      $k_p = \mathrm{argmin}_{m \in \mathcal{M}} \left\|\mathbf{x}_p - \mathbf{p}_m^{(t-1)}\right\|_2^2$
5   *% Representation step*
6   **for** $m = 1, \ldots, M$ **do**
7   **for** $p' = 1, \ldots, P$ **do**
8          $\gamma_{mp'}^{(t)} = \gamma_{mp'}^{(t-1)} +$
         $\mu^{(t)} h^{(t)}(m, k_p) \left(\delta(p - p') - \gamma_{mp'}^{(t-1)}\right)$

9   *% Compute all prototypes*
10   **for** $m = 1, \ldots, M$ **do**
11      $\mathbf{p}_m^{(t)} = \sum_{p=1}^P \gamma_{mp}^{(t)} \phi(\mathbf{x}_p)$

Output: Prototypes $\left\{\mathbf{p}_m^{(T)}\right\}_{m \in \mathcal{M}}$.

It is worth noting that the the output prototypes recovered during this training step can be interpreted as virtual endmember spectra or class representatives for each material present in the observed scene.

2.3 MK-SOM Testing

The MK-SOM testing step of the proposed unmixing algorithm aims at recovering the abundance vector associated to each pixel $\mathbf{y}_n$ ($n = 1, \ldots, N$) of the image to be unmixed. Following a commonly accepted approach [20, 33, 34], the degrees of membership $\{d_{kn}\}_{k=1}^K$ of a testing pixel $\mathbf{y}_n$ to all neurons $\mathbf{p}_m$ are resorted as surrogates of abundances. As in [20], these degrees are finally rescaled to ensure that the final abundance vectors satisfy the widely admitted non-negativity and sum-to-one constraints [2]. The overall process is described in Algo. 2.

Algorithm 2: MK-SOM unmixing: testing step

Input: MK-SOM map $\{\mathbf{p}_k\}_{k \in \mathcal{K}}$, testing vectors $\mathbf{y}_1, \ldots, \mathbf{y}_N$
1 *% Abundance estimation*
2 **for** $n = 1, \ldots, N$ **do**
3   *% Association*
4   **for** $k = 1, \ldots, K$ **do**
5      $d_{kn} = \|\mathbf{y}_n - \mathbf{p}_k\|_2^2$
6   *% Normalization*
7   **for** $k = 1, \ldots, K$ **do**
8      $a_{kn} = \frac{d_{kn}}{\sum_{j=1}^K d_{jn}}$

Output: Abundance vectors $\mathbf{a}_n \triangleq [a_{1n}, \ldots, a_{Kn}]^T$
     ($n = 1, \ldots, N$).

2.4 Initialization

Before beginning the unmixing process, two initialization tasks should be conducted. There are discussed in what follows. First, the spectral signatures of the endmembers to be used in the unmixing process, as well as their number, should be selected. These spectral signatures can be chosen by the practitioner in case of reliable prior knowledge regarding the scene of interest. Otherwise, one may make use of an endmember extraction algorithm already proposed in the literature [35–38]. Note that, as highlighted in [7] and [8], some of these algorithms can provide reliable results to recover endmember from nonlinearly mixed pixels although they initially rely on an implicit linear mixing model. This is, in particular, the case for the geometrical extraction algorithms, such as VCA [12] and N-FINDR [9]. Moreover, note that, in the proposed implementation of the MK-SOM, the number of endmembers is the squared value of the dimension of the SOM weight vectors. However, when this constraint can be fulfilled, any dimension of the SOM weight vectors can be still employed and the resulted map can be post-processed by any unsupervised clustering algorithm (e.g., K-means) to reach the desired number of endmembers [39].

Then, the second task consists in selecting training samples (i.e., hyperspectral pixels) necessary for the training step of the MKL. In [40] and [20], the authors propose to resort to only pure pixels in the training phase, based on the assumption that each pure pixel can be associated with a unique endmember by a degree of membership equals to 1 and with a degree of membership to the other endmembers equal to 0. Instead, tn this work, we propose to define this training set as the outputs of an endmember extraction algorithm, e.g., VCA. Indeed, VCA is able to recover the P most distinct pixels in the considered hyperspectral image. In addition to being unsupervised, this strategy has the great advantage of allowing the learning step of the MK-SOM to be conducted more efficiently since the training set is not limited to actual existing pure pixels in the image. In other words, the training pixels are selected as the P most pure pixels extracted by VCA.

3 Experimental results

To validate the proposed MK-SOM-based unmixing algorithm, its performance has been compared to those obtained by the linear unmixing methods FCLS [13] and SUNSAL [14] and the nonlinear unmixing methods PPNM [16], rLMM [18], K-Hype and its generalized counterpart (SK-Hype) [41]. The experimental datasets consist of synthetic and real images described in what follows.

3.1 Datasets

Firstly, to assess the performance of the unmixing procedures, we consider an hyperspectral image of size 100×100 pixels and composed of 9 endmembers representative of minerals which have been extracted from the U.S. Geological Survey (USGS) spectral library [42]. The abundance maps have been chose as freely available dataset referred to as Fractal 1 and available online [43] has been used. They have been generated according to fractal patterns to ensure realistic distribution of the materials other the scene. In particular, it is constructed such that the pixels nearby the region centers are more spectrally pure than the pixels in the transition areas[44]. Based on these endmembers and abundance maps, the mixed pixels have been generated according to nonlinear model, namely the so-called Fan bilinear model introduced in [45]. An additive white Gaussian noise have been considered with a corresponding signal-to-noise ratio chosen as SNR= 40dB. To illustrate, Fig. 1 depicts the synthetic image in band ♯1.
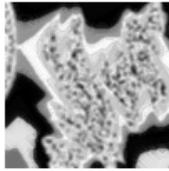

Fig. 1: Band ♯1 of the synthetic image.

Secondly, the real so-called Cuprite dataset acquired by the airborne visible/infrared imaging spectrometer (AVIRIS) has been considered [46]. It consists of a 614×512 pixel image and 224 bands with a spectral range $0.4 - 2.5\mu m$. A set of 33 bands have been removed prior to analysis since they correspond to water absorption band or low SNR. Fig. 2 shows the Cuprite image observed in band ♯10.

Fig. 2: Band ♯10 of the AVIRIS Cuprite image.

3.2 Quality metrics

For the synthetic dataset for which ground-truth (i.e., in terms of actual abundance maps) is available, the performances of the unmixing procedures are evaluated through the mean square error of the abundances [47]

$$\mathrm{MSE}_{\mathbf{A}} = \frac{1}{NK} \sum_{n=1}^{N} \|\hat{\mathbf{a}}_n - \mathbf{a}_n\|_2^2 \tag{13}$$

where $\mathbf{a}_n$ and $\hat{\mathbf{a}}_n$ are the actual and estimated abundance vector associated with the pixel ♯n ($n \in \{1, \ldots, N\}$) and K is the number of endmembers used during the unmixing process.

For the real datasets for which no ground-truth is available, the reconstruction error between the original and recovered pixel signatures [47]

$$\mathrm{RE}_{\mathbf{Y}} = \frac{1}{LN} \sum_{n=1}^{N} \|\hat{\mathbf{y}}_n - \mathbf{y}_n\|_2^2 \tag{14}$$

where $\mathbf{y}_n$ and $\hat{\mathbf{y}}_n$ are the measured and reconstructed spectra associated with the pixel ♯n ($n \in \{1, \ldots, N\}$) and L is the number of spectral bands.

3.3 Results

In the conducted experiments, the proposed MK-SOM unmixing procedure has been implemented with a Gaussian kernel of width equal to 1 since it has shown to outperform outperform linear and polynomial kernels [26]. During the training step, various numbers T_{epoch} of epochs have been considered $T_{\mathrm{epoch}} \in \{20, 35, 50, 100, 200, 500\}$ with the largest size of training sets which equals the number of bands.

Tables 1 and 1 report the performance of the different considered algorithms for a number of endmembers equal to $K = 4$ and $K = 9$, respectively and a $\mathrm{SNR} = 40\mathrm{db}$. These results show that, in case of a number of endmembers equal to 4, the proposed MK-SOM unmixing algorithm consistently outperforms all the other algorithms for any training step parameters (e.g., number T_{epoch} of epochs). The best MSE value (0.0625) is obtained by MK-SOM for a number of epochs equals to $T_{\mathrm{epoch}} = 500$. When the number of endmembers is equal to $K = 9$, the MK-SOM consistently performs better than all other methods. The best MSE value (0.0123) is reached when MK-SOM is run with the number of epochs equal to $T_{\mathrm{epoch}} = 500$.

Table 1 Synthetic dataset ($K = 4$): estimated abundance MSE.

FCLS			0.0982
SUNSAL			0.1039
PPNM			0.1013
rLMM			0.0982
K-Hype			0.0977
SK-HYPE			0.1010
MK-SOM	T_{epoch}	20	0.0626
		35	0.0626
		50	0.0626
		100	0.0626
		200	0.0625
		500	**0.0625**

To illustrate, the corresponding estimated abundance maps for synthetic image are depicted in Fig. 5 for $K = 4$.

As complementary results, Fig. 3 and Fig. 4 report the reconstruction errors for different levels of noise for $K = 4$ and different number of endmembers for $SNR = 40$, respectively.

Similarly, Table 3 shows the performance of compared algorithms when applied to the real AVIRIS Cuprite dataset for a number of endmembers equal to $K = 9$. The proposed MK-SOM consistently outperforms the concurrent methods and, in particular, provides the lowest error for a number of epochs equal to $T_{\mathrm{epoch}} = 20$. To illustrate, the corresponding estimated abundance maps are depicted in Fig. 6 for $K = 4$.

Table 2 Synthetic dataset ($K = 9$): estimated abundance MSE.

FCLS			0.0190
SUNSAL			0.0192
PPNM			0.0189
rLMM			0.0189
K-Hype			0.0181
SK-HYPE			0.0185
MK-SOM	T_{epoch}	20	0.0123
		35	0.0123
		50	0.0123
		100	0.0124
		200	0.0123
		500	**0.0123**
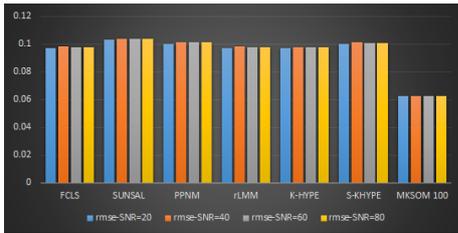
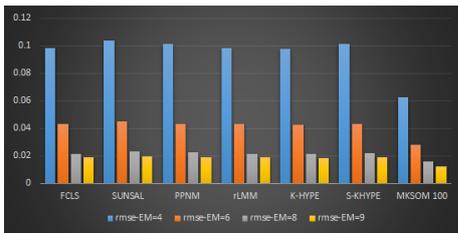**Fig. 3**: Synthetic dataset ($K = 4$): RMSE for SNR $\in \{20, 40, 60, 80\}$.

Fig. 4: Synthetic dataset ($SNR = 40$): RMSE for $K \in \{4, 6, 8, 9\}$.

Table 3 Real AVIRIS Cuprite dataset ($K = 9$): reconstruction error.

FCLS			3.0208
SUNSAL			3.3709
PPNM			2.9808
rLMM			5.8459
K-Hype			3.0093
SK-HYPE			2.9263
MK-SOM	T_{epoch}	20	**2.1544**
		35	2.3510
		50	2.3871
		100	3.2251
		200	3.2602
		500	3.2603

4 Parallel implementation of the MK-SOM algorithm

This section presents a parallel implementation of the MK-SOM algorithm described in Section 2. This implementation is developed on a GPU using a CUDA programming language. The experiments are conducted on a NVidia Tessla N2090 architecture and show that the parallelization provide a significant speedup of the required computational time. *Per se*, MK-SOM learning is a highly parallelized problem as it is based on a SOM learning approach. The complexity of the calculation is greatly affected by SOM map size and number of features (number of bands in the considered unmixing problem). A simple SOM learning can be summarized as Algo. 3.

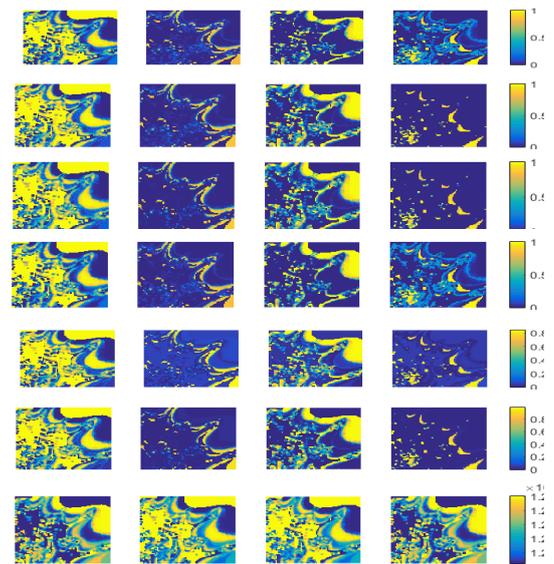The most computationally intensive steps are Steps 3 and 4 of Algo. 3 described below:

Fig. 5: Synthetic dataset ($K = 4$): estimated abundance maps. From top to bottom: FCLS, SUNSAL, PPNM, rLMM, K-Hype, SK-Hype, proposed MK-SOM method. For the proposed MK-SOM algorithm, the abundance maps have been estimated with a $T_{\text{epoch}} = 500$.
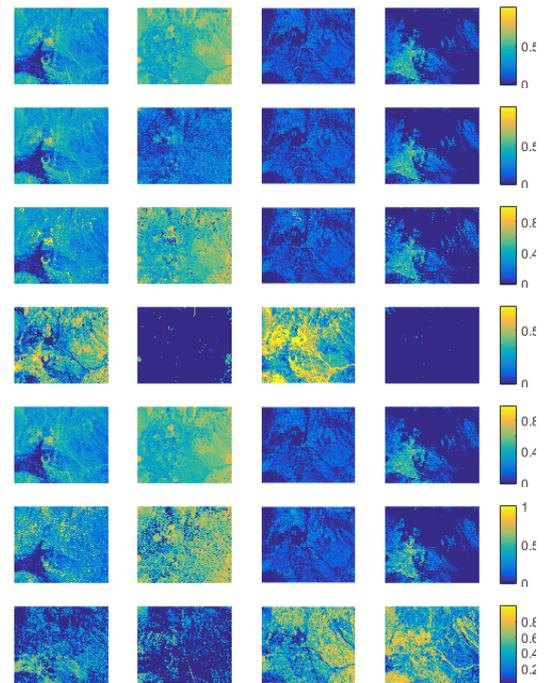

Fig. 6: Real AVIRIS Cuprite dataset ($K = 4$): estimated abundance maps. From top to bottom: FCLS, SUNSAL, PPNM, rLMM, K-Hype, SK-Hype, proposed MK-SOM method. For the proposed MK-SOM algorithm, the abundance maps have been estimated with a $T_{\text{epoch}} = 20$.

• Computing the Euclidean distance between the selected training sample and the SOM map, then obtaining the best matching unit (BMU) which correspond to the minimum distance,
• Updating the SOM map weights according to the distance between the selected training sample and BMU yet updates are limited to only the BMU neighbors.

Algorithm 3: Simple SOM algorithmic sketch.

Initialization:
1 % *Training* **for** $t = 1, \ldots, T$ **do**
2 $\quad$ Select a training sample
3 $\quad$ Get the *best matching unit*
4 $\quad$ Scale neighbors

The degree of parallelism of Step 3 is limited to the dimension of the training set (number of features). On the other hand, the complexity of the MK-SOM testing step (see Section 2.3 and Algo. 2) mainly depends on the image size, the SOM map size and the number of endmembers. Therefore, for a given image, the expected parallelization speedup directly increases with the SOM map size. As an illustrative example of the possible computational gain, the implemented CUDA version has been evaluated in the real AVIRIS Cuprite Image of size $512 \times 614 \times 189$ with different SOM map sizes. The resulting computational times, compared to those obtained on crude (i.e., serial) or multi-threading MATLAB implementations, are reported in Table 4. These results show a significant speedup ranging from $\times 185$ to $\times 6252$ with respect to its MATLAB counterpart. It clear appears that this computation speedup increases as the SOM map size increases. We could also note that the execution time of the serial MATLAB version is exponentially increasing with SOM map size.

Table 4 Real AVIRIS Cuprite dataset: comparison of computational times.

SOM Size	Times(s)			speed
	MATLAB		GPU	
	serial	multi-threaded		
$2 \times 2 \times 189$	108.85	28.025	0.7932	185
$3 \times 3 \times 189$	370.784	27.406	0.6981	531
$10 \times 10 \times 189$	5041.0084	27.663	0.8063	6252

5 Conclusion

This paper introduced a new unmixing method based on simple multiple kernel learning with self-organizing map as a solver. The proposed nonlinear unmixing approach succeeded in reducing the estimation error when applied to synthetic and real hyperspectral images. Moreover, it seemed to be robust with respect to the choice of the parameters required by the training stage. At the price of a slightly more computationally intensive complexity, the proposed MK-SOM framework appears as an relevant alternative of state-of-the art nonlinear unmixing methods. Finally, this paper showed that a parallel implementation of the proposed algorithm was possible. This parallelization was implemented using a graphics processing unit and the resulting computational gain was shown to be highly significant when compared to serial and multi-threaded MATLAB implementations.

Acknowledgment

6 References

1 J. M. Bioucas-Dias, A. Plaza, G. Camps-Valls, P. Scheunders, N. Nasrabadi, and J. Chanussot, "Hyperspectral remote sensing data analysis and future challenges," *IEEE Geosci. Remote Sens. Mag.*, vol. 1, no. 2, pp. 6–36, 2013.

2 J. M. Bioucas-Dias, A. Plaza, N. Dobigeon, M. Parente, Q. Du, P. Gader, and J. Chanussot, "Hyperspectral unmixing overview: Geometrical, statistical, and sparse regression-based approaches," *IEEE J. Sel. Topics Appl. Earth Observations Remote Sens.*, vol. 5, pp. 354–379, Apr. 2012.

3 N. Dobigeon, L. Tits, B. Somers, Y. Altmann, and P. Coppin, "A comparison of nonlinear mixing models for vegetated areas using simulated and real hyperspectral data," *IEEE J. Sel. Topics Appl. Earth Observations Remote Sens.*, vol. 7, pp. 1869–1878, June 2014.

4 I. Meganem, P. Déliot, X. Briottet, Y. Deville, and S. Hosseini, "Linear-quadratic mixing model for reflectances in urban environments," *IEEE Trans. Geosci. Remote Sens.*, vol. 52, pp. 544–558, Jan. 2014.

5 B. Hapke, *Theory of Reflectance and Emittance Spectroscopy*. Cambridge, UK: Cambridge Univ. Press, 1993.

6 R. Heylen, M. Parente, and P. Gader, "A review of nonlinear hyperspectral unmixing methods," *IEEE J. Sel. Topics Appl. Earth Observations Remote Sens.*, vol. 7, pp. 1844–1868, June 2014.

7 N. Dobigeon, J.-Y. Tourneret, C. Richard, J. C. M. Bermudez, S. McLaughlin, and A. O. Hero, "Nonlinear unmixing of hyperspectral images: Models and algorithms," *IEEE Signal Process. Mag.*, vol. 31, pp. 82–94, Jan. 2014.

8 N. Dobigeon, Y. Altmann, N. Brun, and S. Moussaoui, "Linear and nonlinear unmixing in hyperspectral imaging," in *Resolving spectral mixtures – With application from ultrafast time-resolved spectroscopy to superresolution imaging* (C. Ruckebusch, ed.), vol. 30 of *Data Handling in Science and Technology*, pp. 185–224, Oxford, U.K.: Elsevier, 2016.

9 M. E. Winter, "N-FINDR: an algorithm for fast autonomous spectral end-member determination in hyperspectral data," in *Proc. SPIE Imaging Spectrometry V* (M. R. Descour and S. S. Shen, eds.), vol. 3753, pp. 266–275, SPIE, 1999.

10 C.-I Chang, C.-C. Wu, W. min Liu, and Y.-C. Ouyang, "A new growing method for simplex-based endmember extraction algorithm," *IEEE Trans. Geosci. Remote Sens.*, vol. 44, no. 10, pp. 2804–2819, 2006.

11 J. W. Boardman, "Automating spectral unmixing of AVIRIS data using convex geometry concepts," in *Summaries 4th Annu. JPL Airborne Geoscience Workshop*, vol. 1, (Washington, D.C.), pp. 11–14, 1993.

12 J. M. Nascimento and J. M. B. Dias, "Vertex component analysis: A fast algorithm to unmix hyperspectral data," *IEEE Trans. Geosci. Remote Sens.*, vol. 43, no. 4, pp. 898–910, 2005.

13 D. C. Heinz and C.-I Chang, "Fully constrained least squares linear spectral mixture analysis method for material quantification in hyperspectral imagery," *IEEE Trans. Geosci. Remote Sens.*, vol. 39, no. 3, pp. 529–545, 2001.

14 J. M. Bioucas-Dias and M. A. Figueiredo, "Alternating direction algorithms for constrained sparse regression: Application to hyperspectral unmixing," in *Proc. IEEE GRSS Workshop Hyperspectral Image SIgnal Process.: Evolution in Remote Sens. (WHISPERS)*, pp. 1–4, 2010.

15 Y. Altmann, N. Dobigeon, and J.-Y. Tourneret, "Bilinear models for nonlinear unmixing of hyperspectral images," in *Proc. IEEE GRSS Workshop Hyperspectral Image SIgnal Process.: Evolution in Remote Sens. (WHISPERS)*, (Lisbon, Portugal), pp. 1–4, June 2011.

16 Y. Altmann, A. Halimi, N. Dobigeon, and J.-Y. Tourneret, "Supervised nonlinear spectral unmixing using a postnonlinear mixing model for hyperspectral imagery," *IEEE Trans. Image Process.*, vol. 21, no. 6, pp. 3017–3025, 2012.

17 Y. Altmann, N. Dobigeon, and J.-Y. Tourneret, "Unsupervised post-nonlinear unmixing of hyperspectral images using a Hamiltonian Monte Carlo algorithm," *IEEE Trans. Image Process.*, vol. 23, pp. 2663–2675, June 2014.

18 C. Févotte and N. Dobigeon, "Nonlinear hyperspectral unmixing with robust nonnegative matrix factorization," *IEEE Trans. Image Process.*, vol. 24, pp. 4810–4819, Dec. 2015.

19 A. Halimi, J. Bioucas-Dias, N. Dobigeon, G. S. Buller, and S. McLaughlin, "Fast hyperspectral unmixing in presence of nonlinearity or mismodelling effects," *IEEE Trans. Comput. Imag.*, vol. 3, pp. 146–159, Apr. 2017.

20 G. A. Licciardi and F. D. Frate, "Pixel unmixing in hyperspectral data by means of neural networks," *IEEE Trans. Geosci. Remote Sens.*, vol. 49, no. 11, pp. 4163–4172, 2011.

21 B. Ayerdi and M. Graña, "Hyperspectral image nonlinear unmixing and reconstruction by elm regression ensemble," *Neurocomputing*, vol. 174, pp. 299–309, 2016.

22 M. Gönen and E. Alpaydın, "Multiple kernel learning algorithms," *J. Mach. Learning Research*, vol. 12, pp. 2211–2268, 2011.

23 S. Sonnenburg, G. Rätsch, C. Schäfer, and B. Schölkopf, "Large scale multiple kernel learning," *J. Mach. Learning Research*, vol. 7, pp. 1531–1565, 2006.

24 K.-H. Liu, Y.-Y. Lin, and C.-S. Chen, "Linear spectral mixture analysis via multiple-kernel learning for hyperspectral image classification," *IEEE Trans. Geosci. Remote Sens.*, vol. 53, no. 4, pp. 2254–2269, 2015.

25 J. Chen, C. Richard, and P. Honeine, "Nonlinear unmixing of hyperspectral images based on multi-kernel learning," in *Proc. IEEE GRSS Workshop Hyperspectral Image SIgnal Process.: Evolution in Remote Sens. (WHISPERS)*, 2012.

26 Y. Gu, S. Wang, and X. Jia, "Spectral unmixing in multiple-kernel hilbert space for hyperspectral imagery," *IEEE Trans. Geosci. Remote Sens.*, vol. 51, no. 7, pp. 3968–3981, 2013.

27 T. Kohonen and P. Somervuo, "Self-organizing maps of symbol strings," *Neurocomputing*, vol. 21, no. 1, pp. 19–30, 1998.

28 P. Martínez, J. Gualtieri, P. Aguilar, R. Pérez, M. Linaje, J. Preciado, and A. Plaza, "Hyperspectral image classification using a self-organizing map," in *Summaries of the X JPL Airborne Earth Science Workshop*, Citeseer, 2001.

29 M. Olteanu, N. Villa-Vialaneix, and C. Cierco-Ayrolles, "Multiple kernel self-organizing maps," in *Eur. Symp. Artificial Neur. Net., Comput. Intell. Machine Learning*, p. 83, 2013.

30 D. MacDonald and C. Fyfe, "The kernel self-organising map," in *Proc. 4th Int. Conf on Knowledge-Based Intelligent Engineering Systems and Allied Technologies*, vol. 1, pp. 317–320, 2000.

31 N. Villa-Vialaneix and F. Rossi, "A comparison between dissimilarity SOM and kernel SOM for clustering the vertices of a graph," in *Proc. Workshop on Self-Organizing Maps (WSOM)*, (Bielefeld, Germany), pp. WeP–1, 2007.

32 F. Blayo, "Kohonen self-organizing maps: Is the normalization necessary?," *Complex Systems*, vol. 6, no. 6, pp. 105–123, 1992.

33 K. J. Guilfoyle, M. L. Althouse, and C.-I. Chang, "A quantitative and comparative analysis of linear and nonlinear spectral mixture models using radial basis function neural networks," *IEEE Trans. Geosci. Remote Sens.*, vol. 39, pp. 2314–2318, Aug. 2001.

34 Y. Altmann, N. Dobigeon, S. McLaughlin, and J.-Y. Tourneret, "Nonlinear unmixing of hyperspectral images using radial basis functions and orthogonal least squares," in *Proc. IEEE Int. Conf. Geosci. Remote Sens. (IGARSS)*, (Vancouver, Canada), pp. 1151–1154, July 2011.

35 C.-I Chang and Q. Du, "Estimation of number of spectrally distinct signal sources in hyperspectral imagery," *IEEE Trans. Geosci. Remote Sens.*, vol. 42, no. 3, pp. 608–619, 2004.

36 J. Wang and C.-I Chang, "Applications of independent component analysis in endmember extraction and abundance quantification for hyperspectral imagery," *IEEE Trans. Geosci. Remote Sens.*, vol. 44, no. 9, pp. 2601–2616, 2006.

37 J. Wang and C.-I Chang, "Independent component analysis-based dimensionality reduction with applications in hyperspectral image analysis," *IEEE Trans. Geosci. Remote Sens.*, vol. 44, no. 6, pp. 1586–1600, 2006.

38 A. Plaza and C.-I Chang, "Impact of initialization on design of endmember extraction algorithms," *IEEE Trans. Geosci. Remote Sens.*, vol. 44, no. 11, pp. 3397–3407, 2006.

39 J. Vesanto and E. Alhoniemi, "Clustering of the self-organizing map," *IEEE Transactions on neural networks*, vol. 11, no. 3, pp. 586–600, 2000.

40 G. M. Foody, "Relating the land-cover composition of mixed pixels to artificial neural network classification output," *Photogramm. Eng. Remote Sens.*, vol. 62, no. 5, pp. 491–498, 1996.

41 J. Chen, C. Richard, and P. Honeine, "Nonlinear unmixing of hyperspectral data based on a linear-mixture/nonlinear-fluctuation model," *IEEE Trans. Signal Process.*, vol. 61, no. 2, pp. 480–492, 2013.

42 "USGS digital spectral library." http://speclab.cr.usgs.gov/spectral-lib.html. Accessed: 2016-06-17.

43 "HyperMIX: ground truth for fractal images." http://hypercomp.es/hypermix/node/585. Accessed: 2016-06-17.

44 G. Martín and A. Plaza, "Region-based spatial preprocessing for endmember extraction and spectral unmixing," *IEEE Geosci. Remote Sens. Lett.*, vol. 8, no. 4, pp. 745–749, 2011.

45 W. Fan, B. Hu, J. Miller, and M. Li, "Comparative study between a new nonlinear model and common linear model for analysing laboratory simulated-forest hyperspectral data," *International Journal of Remote Sensing*, vol. 30, no. 11, pp. 2951–2962, 2009.

46 "Hyperspectral remote sensing scenes." http://www.ehu.eus/ccwintco/index.php?title = Hyperspectral Remote Sensing Scenes. Accessed: 2016-02-01.

47 J. Plaza, A. Plaza, P. Martínez, and R. Pérez, "H-COMP: A tool for quantitative and comparative analysis of endmember identification algorithms," in *Proc. IEEE Int. Conf. Geosci. Remote Sens. (IGARSS)*, vol. 1, pp. 291–293, 2003.